F. Vignati, A. Guardone
Transition from Regular to Irregular Reflection of Cylindrical Converging Shock Waves over Convex Obstacles
Physics of Fluids, Vol. 29, N. 11, 2017, 116104 (11 pages)
doi:10.1063/1.4989384

Transition from regular to irregular reflection of cylindrical converging shock waves over convex obstacles

F. Vignati, and A. Guardone

Citation: Physics of Fluids **29**, 116104 (2017);
View online: https://doi.org/10.1063/1.4989384
View Table of Contents: http://aip.scitation.org/toc/phf/29/11
Published by the American Institute of Physics

Transition from regular to irregular reflection of cylindrical converging shock waves over convex obstacles

F. Vignati[1,a)] and A. Guardone[2]
[1]*Department of Energy, Politecnico di Milano, Via Lambruschini, 4, 20156 Milano, Italy*
[2]*Department of Aerospace Science and Technology, Politecnico di Milano, Via La Masa, 34, 20156 Milano, Italy*

(Received 8 June 2017; accepted 12 October 2017; published online 22 November 2017)

An analytical model for the evolution of regular reflections of cylindrical converging shock waves over circular-arc obstacles is proposed. The model based on the new (local) parameter, the *perceived wedge angle*, which substitutes the (global) wedge angle of planar surfaces and accounts for the time-dependent curvature of both the shock and the obstacle at the reflection point, is introduced. The new model compares fairly well with numerical results. Results from numerical simulations of the regular to Mach transition—eventually occurring further downstream along the obstacle—point to the perceived wedge angle as the most significant parameter to identify regular to Mach transitions. Indeed, at the transition point, the value of the perceived wedge angle is between 39° and 42° for all investigated configurations, whereas, e.g., the absolute local wedge angle varies in between 10° and 45° in the same conditions. *Published by AIP Publishing.* https://doi.org/10.1063/1.4989384

I. INTRODUCTION

The so-called *reshaping* of shock waves consists in the modification of the shock front shape, following its interaction with a disturbance, e.g., an obstacle or another wave.[1] The reshaping of converging cylindrical or spherical shock waves by means of solid obstacles can prevent the onset of well-known surface instabilities that can reduce the effectiveness of shock waves focusing on, e.g., inertial confinement fusion applications. Shock reshaping via obstacle interaction involves two main physical mechanisms, each of which represents a very interesting challenge.

The first one is the general focusing of converging shock waves. Unlike the case of planar shock waves, indeed, the computation of the solution in the presence of a converging shock wave is more difficult due to, e.g., the non-uniform flow field. Theoretical, experimental, and numerical studies have provided general knowledge on the problem. A milestone was derived independently by Guderley[2] in 1942 and by Butler[3] in 1954 for cylindrical and spherical shock waves, propagating in a non-viscous flow. This relation, hereafter referred to as "Guderley's law," provides a self-similar power law correlating the shock radius and time. This law applies to imploding cylindrical or spherical shock waves in the proximity of the focus axis or point, respectively.

The second mechanism consists in the reshaping of a shock wave. As widely demonstrated by previous studies,[4] depending on the combination between fluid-dynamic properties (the shock Mach number and the gas behavior) and the geometry of the obstacles, diverse types of reflection occur and determine the final shape and stability of the shock. Albeit our understanding of the unsteady interaction between shock waves and solid surfaces is to this day less complete than that of steady reflections, it is well established that such interaction results in a number of peculiar wave systems.[5] The so-called "pseudo-steady" reflections, concerning planar shock waves interacting with planar geometries, may result either in a "Regular Reflection" (RR) or in an "Irregular Reflection" (IR),[6] depending on the only two influential parameters, i.e., the incident shock Mach number and the obstacle wedge angle, both constant. A regular reflection is composed only by the incident shock and the reflected wave, whereas an irregular reflection consists of an additional shock wave and a slip line. The latter group includes "Mach Reflections" (MRs), formed by an incident shock, a reflected wave, and a Mach stem, all intersecting at the so-called "Triple Point" (TP), and a set of non-Mach-type irregular reflections that are observed in the diffraction of weak shock waves over very thin obstacles.[7–11]

As observed in Ref. 5, the extension of pseudo-steady results to the case of cylindrical shock waves interacting with curved obstacles is not straightforward. Indeed, the observed reflection is genuinely unsteady due to the increasing propagation speed of converging shock waves[2,12] and the convexity of both the shock and the obstacle. Moreover, during unsteady reflections, the transition from regular to Mach reflections is observed to occur.[13] Takayama and Sasaki[14] assessed the influence of both the obstacles' curvature radius and the leading edge wedge angle on the transition, in the diffraction of planar shock waves by cylindrical obstacles. The direct comparison between unsteady reflections with the pseudo-steady case allowed Takayama to point out the differences between the two processes. Their analysis was made possible by proving that a class of unsteady shock reflections can be treated as a sequence of pseudo-steady ones, by means of a comparison of the respective polar curves.[15]

This paper explores in detail the reflection of cylindrical converging shock waves over circular-arc obstacles. First, a simple analytical model is derived for describing the propagation of regular reflections and compared to numerical data.

[a)]Electronic mail: federica.vignati@polimi.it

A novel parameter, termed the *perceived wedge angle* θ_w^P, is introduced to account for the local curvatures of both the shock and the obstacle at the reflection point. Then, Takayama's work on the regular-to-Mach transition is extended to the case of cylindrical converging shocks. Starting from regular reflections, the shock evolution is examined until the transition to Mach reflections, which is observed and correlated to the diverse factors.

To assess the model correctness, numerical simulations are performed on a number of configurations, identified by the obstacle thickness-to-chord ratio t/c, leading edge radius r_{LE}, and incident shock Mach number M_s^{LE}. The shock propagates in dilute air, modeled as an ideal gas with constant specific-heat ration $\gamma = 1.4$. Viscous phenomena are assumed to be confined in the boundary layer,[16] whose thickness is considered negligible with respect to the reference scales of the problem.[17] Therefore, results are disengaged from the spatial scale. The software adopted for the numerical simulation of the reflections is the FlowMesh code, a solver for Euler equations developed within the Department of Aerospace Science and Technology of Politecnico di Milano.[18,19]

Section II of this paper includes a brief description of the domain of investigation, i.e., the set of parameters used to identify the reflection, and the features of the numerical simulations, recalling the methodology and the results obtained in Refs. 20 and 21. A simple model describing the evolution of regular reflection is presented and discussed in Sec. III. The model applies to the evolution of the novel parameter θ_w^P while the shock wave propagates along the obstacle, as a function of the local shock Mach number. The dynamic transition from regular to Mach reflections is observed, and the role of the obstacle thickness and radius of curvature is duly discussed in Sec. IV. Conclusions and final considerations are reported in Sec. V. Eventually, the Appendix includes the detailed demonstration of the model equation which describes the evolution of the regular reflection.

II. DESCRIPTION OF THE NUMERICAL EXPERIMENTS

This work stems from the results reported in Ref. 5, which provide a map of the occurrence of the diverse reflection types of cylindrical converging shock waves resulting at the leading edge of circular-arc obstacles. For this reason, the same parameters, computational domain, and numerical features are adopted. The reader is referred to Refs. 5 and 21 for a detailed description of the design of experiments.

A. Geometric parameters and operational conditions

With reference to Fig. 1, unsteady reflections depend on several factors, including the leading edge wedge angle θ_w^{LE}, the incident shock Mach number M_s^{LE}, the obstacle radius of curvature R_o, and the distance of the obstacle leading edge from the focusing point r_{LE}.[5] All the geometrical variables are made dimensionless with the semi-chord length. The focus point of the shock is located at $(0, 0)$. The obstacles are defined as a circular arc whose constant semi-chord is $c = 1$ and whose variable semi-thickness is t. Therefore, the obstacle geometry is fully defined by the parameter t/c only. θ_w^{LE} and R_o both

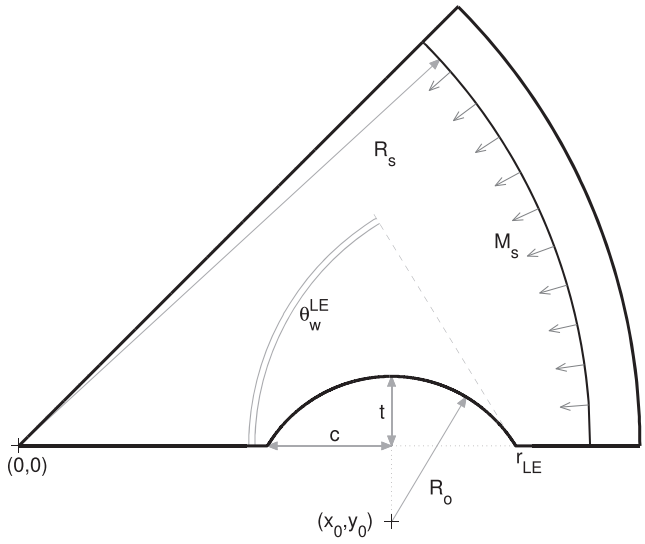

FIG. 1. Extracted from Ref. 5 [F. Vignati and A. Guardone, "Leading edge reflection patterns for cylindrical converging shock waves over convex obstacles," Phys. Fluids **28**, 096103 (2016). Copyright 2016 AIP Publishing LLC.]: Sketch of the computational domain and geometrical features. A half-obstacle is represented, with leading-edge radius r_{LE} and leading-edge wedge angle θ_w^{LE}, depending on the thickness-to-chord ratio t/c. The obstacle profile is a circular-arc, with the center in (x_0, y_0) and radius R_o. The shock is depicted before the reflection, at a radius $R_s > r_{LE}$, converging towards the focus point $(0, 0)$ with a Mach number M_s.

depend only on the value of t/c as follows:

$$R_o = \frac{c}{4}\left(t/c + \frac{1}{t/c}\right),$$
$$\theta_w^{LE} = \frac{1}{2}\left[\pi - \arctan\left(\frac{1}{t/c} - t/c\right)\right]. \tag{1}$$

The computational domain and the geometry are sketched in Fig. 1, reported also in Ref. 5.

In this work, the value of t/c is varied on seven levels, corresponding the latter to the cylindrical case,

$$t/c = 0.07 \cdot (6.5,\ 7,\ 8,\ 9,\ 11,\ 13)\,, 1. \tag{2}$$

The obstacle is located in three positions, corresponding to $r_{LE} = 2.8$, 5.6, and 7.

The shock intensity is described by the value of M_s evaluated at a brief distance upstream the obstacle leading edge. M_s^{LE} evaluated at $r_{LE} = 2.8$ is linearly varied on ten levels, from 2.2 to 6.7. The generation of the shock wave is simulated imposing a circumferential pressure and density step far upstream the obstacle leading edge on still gas, at a radial distance of $10c$ from the focus point. This distance was chosen to guarantee self-similar convergence of the shock waves.[2] The breakup of the initial step profile results in a three-wave system, including a converging shock wave, a contact discontinuity following the shock wave, and a rarefaction wave moving outwards. The internal pressure P_i and density remain constant during the simulations, whereas the initial external pressure is $P_e = \beta_P P_i$. The parameter β_P, namely, the initial pressure ratio, is the controlled parameter to characterize the diverse shock waves. The shock intensity, indeed, is proportional to the value of M_s evaluated at $0.4c$ upstream the obstacle leading edge. The values of β_P are chosen in order to have equally

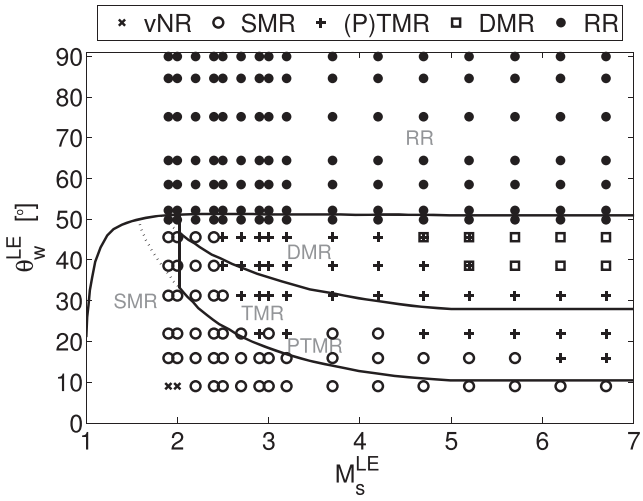

FIG. 2. Extracted from Ref. 5 [F. Vignati and A. Guardone, "Leading edge reflection patterns for cylindrical converging shock waves over convex obstacles," Phys. Fluids **28**, 096103 (2016). Copyright 2016 AIP Publishing LLC.]: Leading edge reflection types. Full lines represent the partition of the plane according to the length-scale criterion for pseudo-steady reflections. The diverse symbols represent different reflection types of converging shock waves over circular-arc obstacles, as observed from numerical simulations. Where two different symbols overlap, it was impossible to clearly determine whether the occurring Mach reflection is transitional or double.

distributed M_s^{LE} over ten levels, from 2.2 to 6.7, evaluated in correspondence with the leading edge of the obstacle located at $r_{LE} = 2.8$. Each of these levels of M_s^{LE}, therefore, corresponds to a value of β_P.

The influence of the leading edge radius r_{LE} on the reflection process is two-fold since it determines the radius of the shock wave and hence its Mach number M_s^{LE} at the point of first interaction. In particular, the lower the value of r_{LE}, the larger the one of M_s^{LE} is.

The choice of these parameters follows from the partition of the plane M_s^{LE}–θ_w^{LE} reported in Fig. 2, extracted from Ref. 5, which allows us to observe the configurations which result in regular reflections at the obstacle leading edge.

The numerical experiments are distributed on a full factorial design,[22] for an overall number of 210 treatments, as reported in Table I.

B. Features of the numerical simulations

Numerical simulations are carried out using the FlowMesh code, developed at the Department of Aerospace Science and Technology of Politecnico di Milano.[18,19] The solver is a standard finite-volume unstructured-grid solver; the unsteady Euler equations for compressible inviscid flows are solved by using a high-resolution flux (centered and Roe scheme, van Leer limiter, see Ref. 23) and by using the backward Euler implicit time integration scheme. The latter is only first-order accurate and was preferred over higher-order backward differentiation formulae for robustness.

TABLE I. Test matrix for the numerical experiments. Considered parameters are the thickness-to-chord ratio t/c, the radial coordinate of the obstacle leading edge r_{LE}, and the initial pressure ratio β_P. In all tests, the operating fluid is air in standard conditions, with $\gamma = 1.4$.

Thickness-to-chord ratio	t/c	0.445, 0.49, 0.56, 0.63, 0.77, 0.91, 1
Chord-normalized leading edge radius	r_{LE}	2.8, 5.6, 7
Initial pressure ratio	β_P	11, 16, 27, 36, 48, 60, 75, 90, 110, 130

Numerical simulations are performed by means of a multi-domain procedure, adopted to reduce the overall computational cost. The method, proposed by the authors, is duly described in Refs. 20 and 21.

References 5 and 21 report an assessment on the adopted space and time discretization. Since the space and time scales of the reflection patterns described in Refs. 5 and 21 are related to the evolution of the regular reflection investigated in this work, the validation of numerical results performed in Refs. 5 and 21 extends to the results presented here. Reference 21 includes also an assessment on the shock wave position in time to verify the accuracy of numerical results.

Therefore, calculations are performed on a fixed grid with normalized node spacing $\Delta x = 0.002$. Hence, the number of nodes of two-dimensional meshes ranges between 200 000 and 500 000 depending on r_{LE}. An *a priori* mesh refinement is performed in correspondence with the obstacle leading edge to capture the details of the shock diffraction. The adopted time step is $\Delta\tau/\tau_{ref} = 1.8 \times 10^{-4}$, where τ_{ref} is the reference time, $\tau_{ref} = c/\sqrt{T_i R}$, where R is the mass-averaged gas constant $R = \mathcal{R}/\sum_{h=1}^{n_c} M_h z_h$, with n_c being the number of components of the gas mixture, M_h being the molecular mass, and z_h being the molar fraction of the hth component. In this work and in Ref. 21, air is modeled as a binary mixture of mostly diatomic gases, i.e., nitrogen (78%) and oxygen (21%) and therefore $R = 287.046$ J/(kg K). The use of implicit schemes in the FlowMesh code[18] allows us to reduce the limitations on the grid spacing due to the Courant-Friedrichs-Lewy (CFL) condition; in all the investigated cases, the ratio $(s\,\Delta\tau)/\Delta x$ is below 0.7, where s is the shock speed.

III. REGULAR REFLECTION EVOLUTION

In the regular reflection of cylindrical shocks over circular-arc obstacles, both the local shock Mach number and the local angle formed by the shock and the reflecting wall change during time, as the shock propagates along the obstacle. Note that in the pseudo-steady case, such an angle is constant. A *perceived wedge angle* θ_w^P is defined here as the angle formed by the obstacle tangent line and the shock radius, both originated from the reflection point.

A. Derivation of the θ_w^P–M_s correlation

An analytical correlation between M_s and θ_w^P is derived in the following, based on geometrical considerations and Guderley's law,[2]

$$R_s = \tilde{r}\left(1 - \frac{\tau}{\tilde{\tau}}\right)^{\alpha}, \tag{3}$$

where α is the self-similarity exponent (characteristic of the problem symmetry and the thermodynamic model) and $\tilde{r}$ and

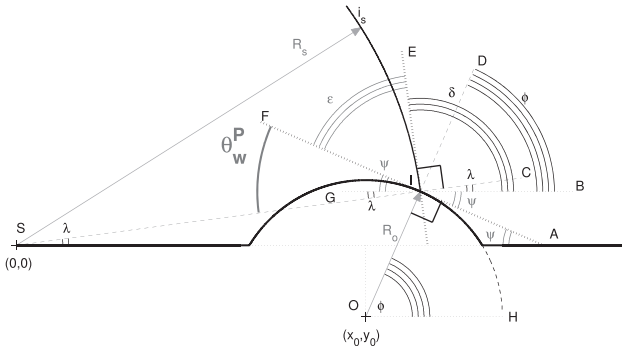

FIG. 3. Definition of the angles adopted in the model of temporal evolution of the combinations θ_w^P–M_s in a regular reflection (the reflected wave is not reported for clearer visibility). The thick solid line represents the reflecting wall, that is, the union of the obstacle and the lower symmetry line. The incident shock wave i_s is represented at a generic radius R_s converging with a Mach number of variable value M_s. The angle θ_w^P is the wedge angle perceived by the shock wave during its convergence, which varies in time to account for the variable slopes of the shock waves and of the obstacle at the reflection point. λ is the azimuthal coordinate of the shock wave in a polar coordinate system. The angle ϕ is the polar angle of the obstacle, centered in the center of the obstacle osculating radius.

$\widetilde{\tau}$ are constants of the problem satisfying the condition

$$\left[\widetilde{r} = r(\tau = 0)\right] \Longleftrightarrow \left[r(\tau = \widetilde{\tau}) = 0\right]. \tag{4}$$

The latter is used to express the local shock Mach number as a function of R_s, whereas geometrical properties allow us to recast angular values to absolute and shock-obstacle relative positions, which are functions of R_s as well. The plane θ_w^{LE}–M_s^{LE}, therefore, can be interpreted as the initial configuration of regular reflections since at the beginning of the reflection $\theta_w^P \equiv \theta_w^{LE}$ and $M_s \equiv M_s^{LE}$. Starting from the leading edge configuration, each regular reflection will propagate on a generic θ_w^P–M_s plane along a trajectory defined by the relation derived in the following.

With reference to Fig. 3, θ_w^P can be expressed as a function of the two angles ϕ and λ as follows:

$$\theta_w^P = \frac{\pi}{2} - \phi + \lambda. \tag{5}$$

These angles represent, respectively, the azimuthal coordinates of the obstacle and of the shock wave in a polar coordinate system. Analytical expressions for ϕ, λ, and θ_w^P are derived in the Appendix and are reported in Table II and marked as Eqs. (A26), (A27), and (A35), respectively.

B. Discussion on the model validity

The relation between the shock position and time by means of Eq. (3) is correct only for genuinely self-similar cases, such as the cylindrical implosion, for which $\alpha = 0.834$ (in polytropic ideal gases).[2,24–27]

It is however well known[14] from approximate theoretical considerations and numerical simulations on cylindrical implosions that for each combination $\left(M_s,\ \theta_w^{LE} \geq \theta_w^{cr}\right)$, there exists a transition angle $\theta_w^{tr} < \theta_w^{cr}$ such that a transition from regular to Mach reflection occurs when $\theta_w^P = \theta_w^{tr}$. It is therefore expected that, regardless of the obstacle thickness and the local shock concavity, $\theta_w^P \approx 0$ if $x_s \approx x_0$. Therefore, the regular reflection must eventually become a Mach reflection. This will cause the shock front to consist of the incident shock i_s and the Mach stem and therefore to depart from the cylindrical shape and from the relation in Eq. (3).

However, also after the RR → MR transition, far from the obstacle the shock shape still obeys axisymmetrical conditions. The perturbation, indeed, propagates along the circumferential direction only up to the triple point: farther from the TP

TABLE II. Complete expression of the angles ϕ, λ, and θ_w^P, which depend on the geometry of the obstacle and are a function of M_s, with $R_s = \widetilde{r}\,(M_s/\widetilde{M_s})^{\frac{\alpha}{\alpha-1}}$ from Eq. (A34).

Angle	Expression	Reference equations
ϕ	$\phi(R_s; x_o, y_o, R_o) = \arccos\left(\dfrac{R_s^2 - x_0^2 - y_0^2 - R_o^2}{2R_o\sqrt{x_0^2+y_0^2}}\right) + \arcsin\left(\dfrac{y_0}{\sqrt{x_0^2+y_0^2}}\right)$	(A26)
λ	$\lambda(R_s; x_o, y_o, R_o) = \arcsin\left\{\dfrac{y_0 + R_o \sin\left[\arccos\left(\dfrac{R_s^2 - x_0^2 - y_0^2 - R_o^2}{2R_o\sqrt{x_0^2+y_0^2}}\right) + \arcsin\left(\dfrac{y_0}{\sqrt{x_0^2+y_0^2}}\right)\right]}{R_s}\right\}$	(A27)
θ_w^P	$\frac{\pi}{2} - \phi(R_s; x_o, y_o, R_o) + \lambda(R_s; x_o, y_o, R_o)$ $= \frac{\pi}{2} - \arccos\left[\dfrac{\left(\frac{M_s}{\widetilde{M_s}}\right)^{\frac{2\alpha}{\alpha-1}}\widetilde{r}^2 - x_0^2 - y_0^2 - R_o^2}{2R_o\sqrt{x_0^2+y_0^2}}\right] - \arcsin\left(\frac{y_0}{\sqrt{x_0^2+y_0^2}}\right)$ $+ \arcsin\left\{\dfrac{y_0}{\left(\frac{M_s}{\widetilde{M_s}}\right)^{\frac{\alpha}{\alpha-1}}\widetilde{r}} + \dfrac{R_o}{\left(\frac{M_s}{\widetilde{M_s}}\right)^{\frac{\alpha}{\alpha-1}}\widetilde{r}} \sin\left\{\arccos\left[\dfrac{\left(\frac{M_s}{\widetilde{M_s}}\right)^{\frac{2\alpha}{\alpha-1}}\widetilde{r}^2 - x_0^2 - y_0^2 - R_o^2}{2R_o\sqrt{x_0^2+y_0^2}}\right] + \arcsin\left(\dfrac{y_0}{\sqrt{x_0^2+y_0^2}}\right)\right\}\right\}$	(A35)

position, the shock remains cylindrical. Therefore the overall time-to-focusing $\widetilde{\tau}$ and convergence rate α remain the same. In case of more than one obstacle, the model fails because the multiple Mach reflections—two for each obstacle—would influence all the shock front shape, as it is in the case of multiple obstacle configurations, inducing the so-called *shock reshaping*.[28] It was however verified[29] that if the reshaped shock conserves a high level of symmetry (i.e., if obstacles are symmetrically arranged along the azimuth so that the reshaped shock is a symmetric polygon), the shock position with respect to time still follows a power-law trend, even though with different α, $\widetilde{r}$, and $\widetilde{\tau}$ constants. Moreover, the higher the number of edges of the polygon, the closer the propagation will follow that of the axisymmetric cylindrical shock in terms of values of α, $\widetilde{r}$, and $\widetilde{\tau}$, as observed in Refs. 21 and 29. In this framework, it is assumed that the values of the three constants do not vary with respect to the axisymmetric problem and that therefore the effect of the RR → MR transition on these parameters can be neglected.

C. Comparison of Eq. (A35) with numerical results

The accordance of the analytic law (A35) with the numerical results is reported in Fig. 4, concerning a regular reflection over one circular obstacle. The local Mach number of the shock is measured by means of the procedure described in Ref. 21. In Fig. 4, the time is increasing from top ($\theta_w^{LE} = \pi/2$) to bottom ($\theta_w^{LE} > 0$ when $\phi = \pi/2$). During the evolution of the regular reflection, θ_w^P spans from θ_w^{LE} to the value of the perceived angle where the regular reflection terminates and the transition into a Mach reflection occurs.

The average trajectory along the θ_w^{LE}–M_s plane agrees fairly well with the numerical prediction, even though dispersion of the sampled values is observed. The error is possibly due to the technique adopted to evaluate the value of M_s from the numerical simulations. Indeed, the latter is assumed to be proportional to the difference between the shock radii at different time steps, and therefore the error on M_s includes the

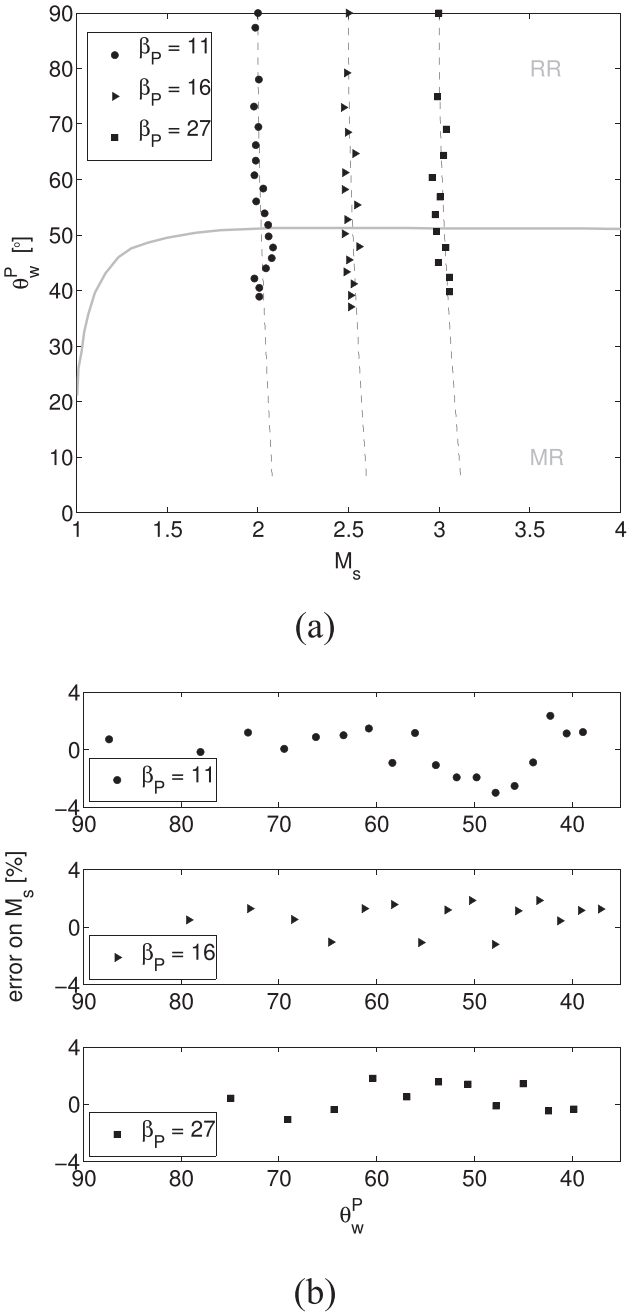

FIG. 4. Predicted evolution of M_s and θ_w^P in regular reflections according to Eq. (A35). (a) Predicted evolution of M_s and θ_w^P in regular reflections (dashed line) and numerical results (•, ▸, ■) for diverse initial conditions. Time increases from top to bottom. (b) Percentage deviation between theoretical and numerical values.

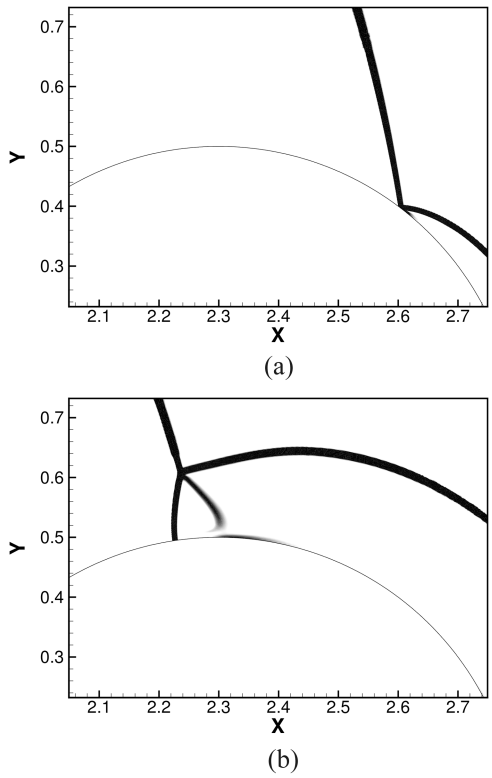

FIG. 5. Transition from (a) regular reflection to (b) Mach reflection for a shock wave impinging on a cylindrical obstacle with $M_s = 2.0$ ($\beta_P = 11$) at $r_{LE} = 5.6$. The shock wave configuration during the transition reproduces the well-known case of RR → MR transition investigated by Takayama and Sasaki[14] and Heilig.[31]

contributions of two measurements and propagates towards the following time step.

A persistence of regular reflections is observed for $\theta_w^{LE} < \theta_w^{cr}$, in accordance with the observations performed in Ref. 14.

IV. NON-LEADING EDGE TRANSITIONS

As observed by several theoretical and experimental studies dealing with the reflection of weak planar shocks over cylindrical obstacles,[14,30,31] due to the loss of self-similarity with respect to the pseudo-steady problem, θ_w^P varies along time, and therefore the reflection may possibly change from regular to Mach type during the shock propagation. Authors assessed the effect of the initial wedge angle and the radius of curvature of the obstacle.

In this work, the RR ⟶ MR transition is observed also for cylindrical shocks. Figure 5 reports the temporal evolution of the reflection pattern of a shock wave generated by an initial pressure ratio $\beta_P = 11$. The shock with $M_s^{LE} = 2.0$ undergoes a transition from a regular reflection to a Mach type one.

In the following, the RR ⟶ MR transition will be discussed for obstacles which can produce a regular reflection at the leading edge. With reference to numerical results reported in Fig. 2, a regular reflection occurs for obstacles with $t/c = 0.445$, 0.49, 0.56, 0.63, 0.77, 0.91, and 1.0.

Figure 6 illustrates the RR ⟶ MR transition points along the obstacle profile. On each picture, data indicated with the same marker represent reflections over obstacles with a common r_{LE} value, regardless of the value of the shock Mach number. The detection of the transition points was achieved by means of simple visual observation of the computed flow fields and did not require the development of an automatic procedure. For each analyzed configuration, the value of the coordinates of the transition point (x^{tr}, y^{tr}) is sampled. The *absolute transition angle* θ_w^{tr} is defined here as the angle between the local obstacle tangent line and the chord direction. θ_w^{tr}, therefore, is evaluated as

$$\theta_w^{tr} = \frac{\pi}{2} - \arctan\left(\frac{y^{tr} + y_0}{x^{tr} - x_0}\right). \tag{6}$$

The perceived transition angle $\theta_w^{tr,P}$ and the local shock Mach number at the transition are calculated by means of Eq. (A35).

From Fig. 6, one observes that the larger the value of t/c, the lower the value of θ_w^{tr} and that the larger the value of r_{LE}, the higher the value of θ_w^{tr} is. The effect of r_{LE} is in accordance with reference results because the reflection of weak planar shocks over convex obstacles represents a limit of the present case, that is, for $r_{LE} \longrightarrow \infty$.

The main error source in the measurement can be attributed to the observation that, immediately after the RR ⟶ MR transition, the growth of the Mach stem is much slower than during the following evolution of the Mach reflection; this makes it difficult to detect the transition of the regular reflection into the Mach reflection, resulting in a maximum measurement error of ±2.0° in the determination of θ_w^{tr} and, therefore, $\theta_w^{tr,P}$.

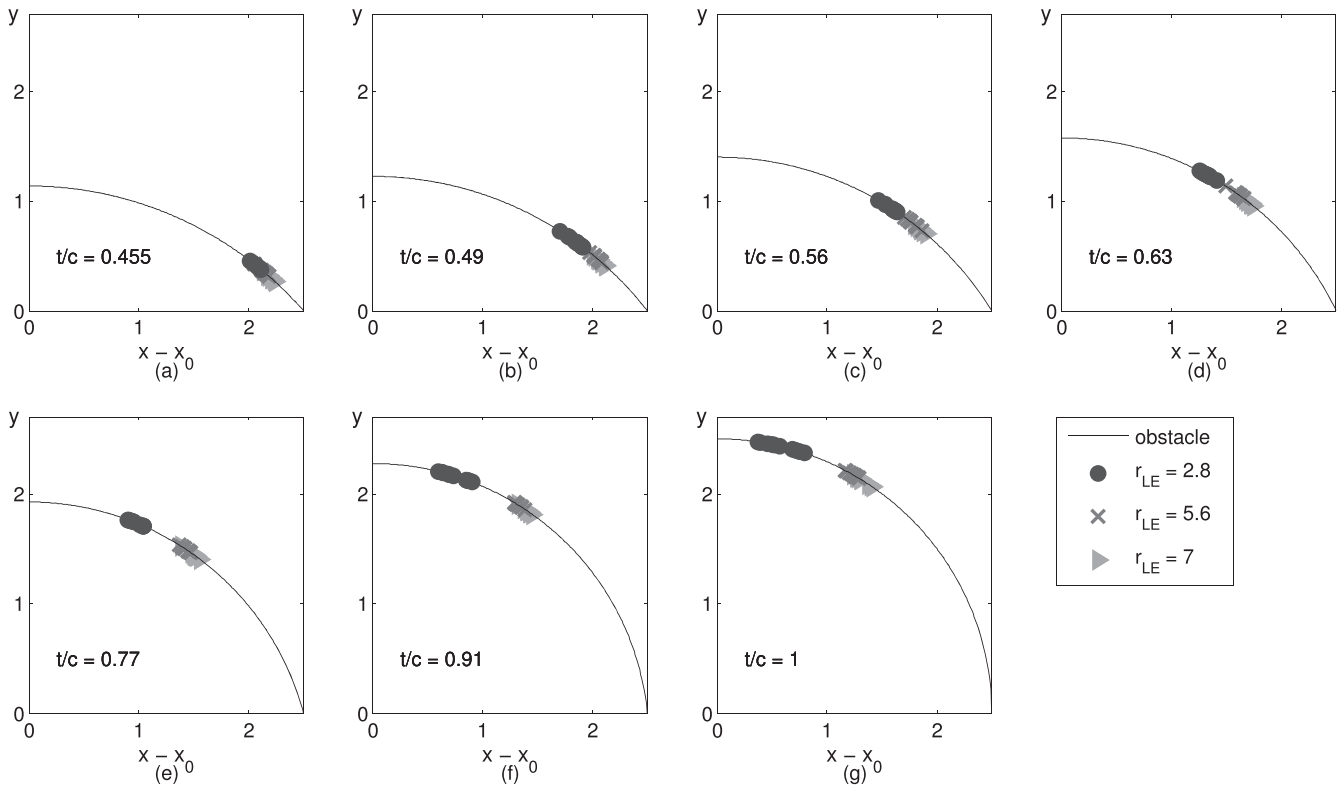

FIG. 6. RR ⟶ MR transition for increasing t/c and r_{LE}: $r_{LE} = 2.8$ (●), $r_{LE} = 5.6$ (×), and $r_{LE} = 7$ (▸). On each picture, data indicated with the same marker represent reflections over obstacles with a common r_{LE} value but different shock Mach numbers.

In Fig. 7, the effect of the shock Mach number is shown.

Each row of the array of pictures in Fig. 7 is associated with a diverse r_{LE} value. The left column represents the transition points in terms of global quantities, i.e., θ_w^{tr} and M_s^{LE}. On the contrary, the pictures on the right column depict the local values of wedge angle $\theta_w^{tr,P}$ and M_s at the transition. Each line represents the transition angle as a function of the shock Mach number for a diverse obstacle t/c.

With reference to Figs. 7(a), 7(c), and 7(e) (left column of Fig. 7), it is observed that the absolute θ_w^{tr} is affected mainly by the obstacle thickness and less by the shock intensity, as in the self-similar case.[14] Indeed, from Fig. 7, no evident trend can be highlighted due to the effect of the shock Mach number. On the contrary, for a given combination of r_{LE} and β_P, it can be observed that, in general, the larger the value of t/c, the lower the value of θ_w^{tr} is. Therefore, the existence of a regular reflection in the presence of wedge angles which would generate leading edge Mach reflections is more relevant for larger t/c values. Under the qualitative point of view, the effect of r_{LE} is found to influence the range of variability of the transition angles for diverse t/c values: θ_w^{tr} ranges about from 10° to 40° for $r_{LE} = 2.8$, from 27° to 41° for $r_{LE} = 5.6$, and from 30° to 43° for $r_{LE} = 7$.

The dependence of θ_w^{tr} on t/c can be expressed in terms of R_o and θ_w^{LE}, in accordance with Eq. (1). In particular, θ_w^{tr} is higher if R_o is larger and therefore if θ_w^{LE} is smaller. The first result—the relation between the transition angle and the obstacle curvature—is in accordance with the observations in Refs. 14 and 30 on the reflection of planar shock waves over convex obstacles. In these studies, indeed, an increasing trend between R_o and θ_w^{tr} was observed. The second result, i.e., the decreasing trend between θ_w^{LE} and θ_w^{tr}, seems to differ from the results of Ref. 14 where, on the contrary, an increasing trend between θ_w^{LE} and θ_w^{tr} was observed. In the cited reference, however, the effects of R_o and θ_w^{LE} were assessed independently. On the contrary, in this work, both R_o and θ_w^{LE} are accounted for via the parameter t/c, and therefore their influence cannot be observed separately.

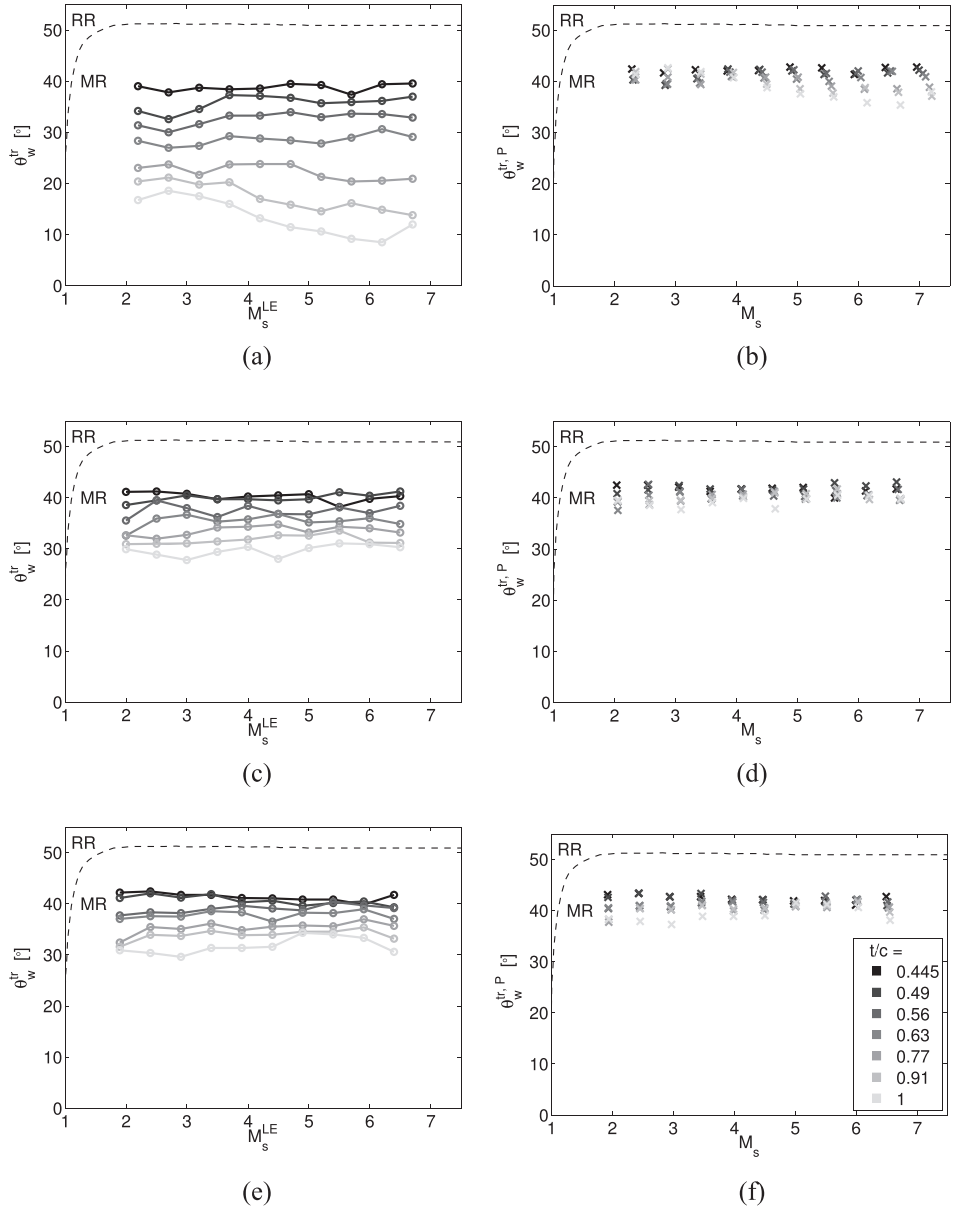

FIG. 7. Transition angles versus shock Mach number parametrized on t/c and r_{LE}: absolute values (left column, ⊸) and values perceived at the transition (right column, ✕).

If local values of the wedge angle and shock Mach number are considered, i.e., the perceived angle $\theta_w^{tr,P}$ and the transition M_s [Figs. 7(b), 7(d), and 7(f), the right column of Fig. 7], the contribution due to t/c is significantly weaker than in the case of the absolute transition angle. $\theta_w^{tr,P}$ becomes independent from the values of both M_s^{LE} and t/c. Moreover, the effect of r_{LE} becomes almost negligible since the range of variability of $\theta_w^{tr,P}$ remains the same—about from 37° to 43°—for all the diverse investigated r_{LE} values.

Unlike geometric factors, the shock Mach number appears to have a weak or negligible influence on both the values of θ_w^{tr} and of $\theta_w^{tr,P}$ in the considered range of parameters. Therefore, to better assess the effects of the most relevant factors, i.e., t/c and r_{LE}, on the RR ⟶ MR, the Mach number will be neglected in the following analysis. In Fig. 8, each point of the diagram represents the average transition angle for a given combination of t/c and r_{LE}, which is computed on the average value for all M_s^{LE}. The absolute and the perceived transition angles are represented in Fig. 8(a) and Fig. 8(b), respectively. For each obstacle geometry (combination of t/c and r_{LE}), the range of variability of the transition angle due to the shock Mach number is represented by a vertical bar centered in the mean value of θ_w^{tr}.

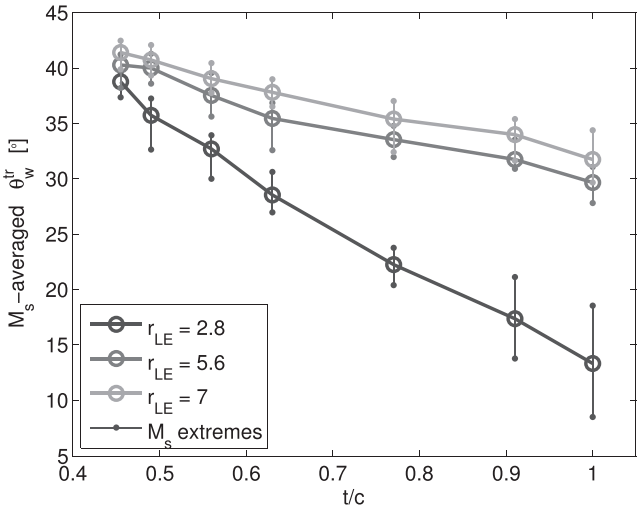

(a)

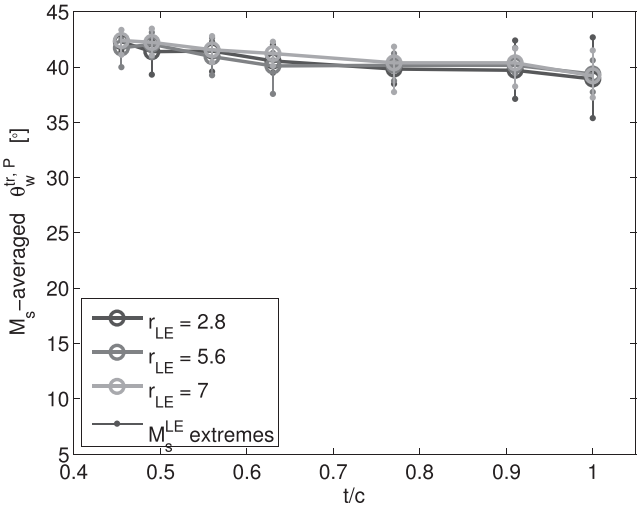

(b)

FIG. 8. Average (a) absolute and (b) perceived transition angles versus t/c and parametrized on r_{LE} (⊸). For each point, the range of variability due to M_s is indicated by the bar ⊥.

As observed above, θ_w^{tr} exhibits a monotonically decreasing trend versus t/c, whose average slope is influenced by r_{LE}.

On the contrary, $\theta_w^{tr,P}$ does not present a significant dependence on t/c, being the average slopes of the curves almost null. Moreover, all the three curves associated with the three values of r_{LE} become completely overlapped. The above indicates that $\theta_w^{tr,P}$ is not influenced by r_{LE}, that is, the shock curvature, to a first degree of approximation.

The weak dependence of $\theta_w^{tr,P}$ on all the other parameters, i.e., t/c, M_s, and r_{LE}, suggests that the perceived wedge angle is the most significant parameter to identify regular to Mach transitions.

V. CONCLUSIONS

Numerical simulations were performed to investigate the evolution of the regular reflection of cylindrical converging shock waves over circular-arc obstacles. The adopted gas was air in dilute conditions, and a constant specific-heat ratio was assumed. Two solvers for Euler equations are used to compute the solution, the first being in one-dimensional axisymmetrical form—for the simulation of the cylindrical shock onset and propagation—and the second one in the two-dimensional Cartesian formulation for the simulation of the shock-obstacle interaction. A multi-domain procedure was set up to compute the interface between the two solutions.

The novel parameter *perceived wedge angle* was introduced to account for the unsteady evolution of the curvatures of both the shock wave and the obstacle at the reflection point. A model for the description of regular reflections was developed, which allows us to trace the combinations of the local M_s and the perceived local wedge angle θ_w^P during the shock propagation in time. The value of θ_w^P predicted by the model is in good accordance with numerical results.

The value of θ_w^P changes during the shock convergence, and therefore a transition from regular reflection to Mach reflection is observed. The combination between the wave Mach number M_s of the incident shock and the local wedge angle θ_w^{tr} which triggers the transition is computed for the first time for diverse values of the parameter t/c, which includes the effects of both the leading edge wedge angle and the obstacle radius of curvature R_o. This allows a comparison with the literature, showing good agreement in the trend between θ_w^{tr} and R_o, but a discording one between θ_w^{tr} and θ_w^{LE} with respect to Ref. 14. Since the present work adopts a different set of variables with respect to the work of Takayama and Sasaki,[14] it is not clear whether the latter poor agreement is due to different phenomenology or due to the stronger effect of R_o rather than θ_w^{LE} in the case of converging shock waves.

Numerical results suggest that the new parameter θ_w^P is likely the most important parameter to describe the evolution of the regular reflections and their evolution into Mach reflections. Indeed, $\theta_w^{tr,P}$, i.e., θ_w^P at the transition, is between 39° and 42° regardless of t/c, M_s, and r_{LE}, whereas the classical

parameter θ_w^{tr} is in between 10° and 45°. This allows us to empirically define for the first time a geometrical invariant, i.e., θ_w^P, within the unsteady reflection framework.

A final remark concerns the range of validity of the proposed results. It is worth noticing, indeed, that results reported in this work have been derived under strong assumptions, and therefore they represent an empirical description of cylindrical shock reflections over circular-arc obstacles. In the detail of the RR ⟶ MR transition, indeed, the dependence of the transition angle on the shock Mach number is assumed to be a second-order effect, and therefore it was not further investigated. On the contrary, the advantage of this approach is that it covers the whole range of admissible obstacle thickness: with reference to Fig. 2, for $M_s^{LE} \approx 2$ and higher, the dependence of θ_w^{cr} on the incident shock Mach number is negligible, possibly null. Therefore, the effects of all the possible t/c values which generate a leading edge regular reflection are fully explored in Secs. III and IV.

This implies that the correlations derived in Secs. III and IV can be adopted even if they are known in advance to provide only a phenomenological description. The reason is that their predictive ability is expected to be fairly good albeit their simpleness because the domain on which they can be applied is coincident with the one used to define them.

The only parameter whose effect is neglected, due to its weak effect, is the (local or incident) shock Mach number. However, for shocks stronger than the explored ones, high temperature effects become non-negligible, and therefore the polytropic ideal gas model cannot apply. On the contrary, if weaker shocks are considered, it is necessary to keep into account that the physics of weak shock reflections[32] is much more complex than the one used to describe regular and Mach reflections, and the required computational resources increase, too.[33] Therefore, different computational methods and assumptions would be required to describe the reflection of weak or very strong shocks. In conclusion, it is the authors' opinion that the domain of shock Mach numbers where the proposed correlations are valid cannot be further extended.

APPENDIX: ANALYTICAL EXPRESSION FOR ANGLES

In this appendix, the analytical expressions for the angles ϕ, λ, and θ_w^P in Table II are derived.

The angles ϕ and λ are reciprocally linked through the generic angles δ and ψ as in Fig. 3. The latter two are the angles formed with the obstacle chord—i.e., the horizontal axis—by the lines tangent, respectively, to the shock wave and to the obstacle at the reflection point, named *I*. ε is a dummy angle used only for the derivation of Eq. (5). The two points S and O indicate the focus point and the center of the obstacle osculating circle, respectively. Other Latin uppercase letters in Fig. 3 are dummy variables used to indicate reference points used to define the angles. The model purpose is to correlate θ_w^P and M_s in a regular reflection, and therefore it is valid for $\phi \in \left[\phi^{LE}, \frac{\pi}{2}\right]$.

With reference to the nomenclature introduced in Fig. 3, the line $\overline{IE}$ is the tangent line to the shock wave at the reflection point. $\overline{SI}$ connects the focus point to the reflection point, and therefore it is also a radius of the circumference representing the incident shock wave i_s. For this reason, the two segments $\overline{SI}$ and $\overline{IE}$ are perpendicular. The line $\overline{FI}$ is the tangent line of the obstacle at the reflection point I and divides the right angle $\widehat{SIE}$ into two parts. Therefore, θ_w^P is the complementary of the angle $\widehat{FIE}$, termed ε,

$$\overline{SI} \perp \overline{IE} \implies \theta_w^P = \frac{\pi}{2} - \varepsilon. \tag{A1}$$

The point A is in the intersection between the line $\overline{FI}$ and the lower symmetry line. Therefore, the points F, I, and A belong to the straight line $\overline{FA}$. The segment $\overline{IB}$ is a horizontal line passing by the reflection point. Therefore, the angle $\widehat{FIA} = \pi$ can be expressed as the sum of three angles, i.e., ε, $\widehat{BIA}$, and their supplementary, named δ,

$$\widehat{FIA} = \pi \implies \varepsilon = \pi - \delta - \widehat{BIA}. \tag{A2}$$

The two lines $\overline{SA}$ and $\overline{IB}$ are parallel by definition, and they are crossed by the line $\overline{IA}$. The two angles $\widehat{BIA}$ and $\widehat{IAS}$ are alternate interior angles, and therefore they have equal values. For this reason, they will be both referred to as ψ,

$$\overline{IB} \parallel \overline{SA} \implies \widehat{BIA} = \widehat{IAS} =: \psi. \tag{A3}$$

The combination of Eqs. (A2) and (A3) provides the expression of ε as a function of δ and ψ,

$$\varepsilon = \pi - \delta - \psi. \tag{A4}$$

It is now necessary to evaluate the angles δ and ψ. The line $\overline{DI}$ is adjacent to the line $\overline{OI}$, which is the radius of the obstacle passing by the reflection point. For this reason, the lines $\overline{DI}$ and $\overline{IA}$ are perpendicular, and the line $\overline{IB}$ subdivides the right angle $\widehat{DIA}$ into two,

$$\overline{DI} \perp \overline{IA} \implies \psi = \frac{\pi}{2} - \widehat{DIB}. \tag{A5}$$

Since $\overline{IB}$ and $\overline{OH}$ are the horizontal lines, the two angles $\widehat{DIB}$ and $\widehat{IOH}$ are the corresponding angles of the two parallel lines $\overline{IB}$ and $\overline{OH}$ cut by the transversal line $\overline{DO}$. Therefore, $\widehat{DIB}$ and $\widehat{IOH}$ are the equal angles of value ϕ,

$$\overline{OH} \parallel \overline{IB} \implies \widehat{DIB} = \widehat{IOH} =: \phi. \tag{A6}$$

Equations (A5) and (A6) provide the correlation between the dummy angle ψ and the obstacle polar angle ϕ,

$$\psi = \frac{\pi}{2} - \phi. \tag{A7}$$

The other angle used to define ε, i.e., δ, corresponds to the angle between the segments $\overline{IB}$ and $\overline{EI}$. The angle $\widehat{EIB}$ is crossed by the segment $\overline{IC}$ and subdivided into the two angles $\widehat{EIC}$ and $\widehat{CIB}$. Moreover, $\overline{IC}$ is also adjacent to $\overline{SI}$ and therefore perpendicular to the shock tangent line $\overline{EI}$. For this reason, the angle δ is obtained by the sum of the right angle $\widehat{EIC}$ and the angle $\widehat{CIB}$,

$$\overline{EI} \perp \overline{IC} \implies \delta = \frac{\pi}{2} + \widehat{CIB}. \tag{A8}$$

The horizontal lines $\overline{IB}$ and $\overline{SA}$ are cut by the transversal line $\overline{BS}$, which defined the corresponding—and therefore congruent—angles $\widehat{CIB}$ and $\widehat{ISA}$. The latter is the shock polar angle λ and therefore also $\widehat{CIB} = \lambda$,

$$\overline{IB} \parallel \overline{SA} \implies \widehat{CIB} = \widehat{ISA} =: \lambda. \tag{A9}$$

This result, together with the expression of δ from Eq. (A8), correlates the dummy variable δ with the polar coordinate of the shock evaluated at the reflection point λ,

$$\delta = \frac{\pi}{2} + \lambda. \tag{A10}$$

The correlation between the angle ε and the two polar angles is obtained by substituting the expressions of ϕ and λ [provided by Eqs. (A7) and (A10)] in Eq. (A4),

$$\left.\begin{aligned} \varepsilon &= \pi - \delta - \psi \\ \delta &= \frac{\pi}{2} + \lambda \\ \psi &= \frac{\pi}{2} - \phi \end{aligned}\right\} \Longrightarrow \varepsilon = \phi - \lambda. \tag{A11}$$

Finally, the expression of ε as a function of ϕ and λ is used to define the perceived wedge angle θ_w^P,

$$\theta_w^P = \frac{\pi}{2} - \phi + \lambda. \tag{A12}$$

The correlation between geometrical and kinematic parameters follows from the parametrization in polar coordinates of the shock wave (whose geometry is time dependent) and the obstacle (which is fixed, instead), by means of ϕ and λ,

$$\text{Obstacle:} \qquad \overline{z_o} = \begin{cases} x_o = x_0 + R_o \cos\phi, \\ y_o = y_0 + R_o \sin\phi, \end{cases} \tag{A13}$$

$$\text{Shock:} \qquad \overline{z_s} = \begin{cases} x_s = R_s(\tau) \cdot \cos\lambda, \\ y_s = R_s(\tau) \cdot \sin\lambda. \end{cases} \tag{A14}$$

At point I, where the shock and the obstacle intersect, their coordinates are coincident, i.e., $\overline{z_s} = \overline{z_o}$,

$$\begin{cases} x_0 + R_o \cos\phi = R_s \cos\lambda, \\ y_0 + R_o \sin\phi = R_s \sin\lambda. \end{cases} \tag{A15}$$

Equation (A15) contains three unknowns R_s, λ, and ϕ. In this framework, R_s is not known because the goal is not the determination of the shock position at a given time, but the definition of a correlation describing a temporal evolution, and therefore $R_s(\tau)$ must be considered an unknown variable.

The squares of the right- and left-hand sides of each row of the system $\overline{z_s} = \overline{z_o}$ [Eq. (A15)] are computed, and the rows of $(\overline{z_s})^2 = (\overline{z_o})^2$ are added,

$$\begin{aligned} x_0^2 + y_0^2 + R_o^2 \underbrace{\left(\cos^2\phi + \sin^2\phi\right)}_{1} + 2R_o \underbrace{(x_0\cos\phi + y_0\sin\phi)}_{f(\phi)} \\ = R_s^2 \underbrace{\left(\cos^2\lambda + \sin^2\lambda\right)}_{1}. \end{aligned} \tag{A16}$$

The Pythagorean identity allows us to drop the mutual dependence of ϕ and R_s from λ. Moreover, as resulting from Eq. (A16), all the terms containing the unknown ϕ are merged in the generic expression $f(\phi)$ and disengaged from the remaining unknown R_s. Therefore, Eq. (A16) is manipulated to separate $f(\phi)$, in the left-hand side, from R_s in the right-hand side,

$$f(\phi) = (x_0\cos\phi + y_0\sin\phi) = \frac{R_s^2 - x_0^2 - y_0^2 - R_o^2}{2R_o}, \tag{A17}$$

where $f(\phi)$ is decomposed into the product of two terms, the variables q and q'. The latter is defined as

$$q' := \sqrt{x_0^2 + y_0^2}, \tag{A18}$$

and therefore $f(\phi)/q'$ is rewritten as

$$\frac{x_0}{q'}\cos\phi + \frac{y_0}{q'}\sin\phi =: q. \tag{A19}$$

Since

$$\frac{x_0^2}{q'^2} + \frac{y_0^2}{q'^2} = 1, \tag{A20}$$

a dummy variable ν is introduced that satisfies the following relation:

$$\left(\frac{x_0}{q'}, \frac{y_0}{q'}\right) = (\cos\nu, \sin\nu). \tag{A21}$$

Therefore, the variable q is rewritten as a function of ϕ [from Eq. (A19)] and ν [from Eq. (A21)] in the compact form provided by addition formulas,

$$\begin{aligned} q &= \cos\nu\cos\phi + \sin\nu\sin\phi \\ &= \cos(\pm(\phi - \nu)). \end{aligned} \tag{A22}$$

By reversing the dependence of the variables in Eq. (A22) and maintaining both the positive and the negative arguments in the cosine, one has

$$\phi = \pm\arccos(q) + \nu. \tag{A23}$$

The sign of ϕ is determined as follows: the ordinate of the obstacle osculating circle is negative, and therefore $\sin\nu$ and ν are also negative. On the contrary, $\phi \geq 0$ for definition because the obstacle is described by a polar angle $\phi \geq \phi^{LE}$. For this reason, from Eq. (A23), one has

$$\pm\arccos(q) = \phi - \nu \geq 0. \tag{A24}$$

The codomain of the arccosine function is non-negative for definition, i.e.,

$$\arccos(\omega) \geq 0 \quad \forall\omega \in [-1, 1], \tag{A25}$$

and therefore the positive solution is accepted, i.e., $\arccos(q) \geq 0$. By recalling the definitions of q [Eq. (A19)] and ν [Eq. (A21)], ϕ is explicitly correlated to R_s (see Table II for the complete expression of ϕ),

$$\phi = \arccos(q) + \arcsin\left(\frac{y_0}{q'}\right). \tag{A26}$$

The expression of λ is obtained substituting Eq. (A26) into Eq. (A15) (see Table II for the complete expression of λ),

$$\lambda = \arcsin\left(\frac{y_0 + R_o\sin\phi}{R_s}\right). \tag{A27}$$

With this expression, ϕ and λ are functions only of R_s and are parametrized on the obstacle geometry. Combining Eq. (5) with Eqs. (A26) and (A27), the expression is obtained for $\theta_w^P = \theta_w^P(R_s;\ \text{obstacle geometry})$.

To express $R_s = R_s(M_s)$, Guderley's self-similar law applies to describe the position of the cylindrical shock versus time for a given set of initial conditions,

$$R_s = \tilde{r}\left(1 - \frac{\tau}{\tilde{\tau}}\right)^{\alpha}, \tag{A28}$$

where α, $\tilde{r}$, and $\tilde{\tau}$ are constants defined in Sec. III.

Provided $R_s(\tau)$ by means of Guderley's model, the shock speed s is computed as the time derivative of R_s,

$$s = \dot{R}_s = \widetilde{r}\alpha\left(1-\frac{\tau}{\widetilde{\tau}}\right)^{\alpha-1}\cdot\left(-\frac{1}{\widetilde{\tau}}\right) = \underbrace{\widetilde{r}\left(1-\frac{\tau}{\widetilde{\tau}}\right)^{\alpha}}_{R_s}\cdot\frac{-\alpha}{\widetilde{\tau}\left(1-\frac{\tau}{\widetilde{\tau}}\right)}$$

$$= R_s\cdot\frac{-\alpha}{\widetilde{\tau}-\tau}, \tag{A29}$$

and its Mach number is calculated as

$$M_s = \frac{\left|\dot{R}_s\right|}{a_i} = R_s\cdot\frac{\alpha}{a_i\left(\widetilde{\tau}-\tau\right)}, \tag{A30}$$

where a_i is the speed of sound in the internal reason.

If the initial time is set in correspondence with the shock impingement, the value of $\widetilde{r}$ is known but $\widetilde{\tau}$ is not since it depends on the evolution of the shock. However, in the following, it will be assumed that $\widetilde{\tau}$ is very close to the one of a cylindrical shock (the validity of this approximation is discussed in Sec. III B) and that therefore $\widetilde{\tau}$ can be calculated as follows:

$$\left.\begin{aligned}\widetilde{M_s} &= M_s|_{\tau=0}\\ \widetilde{r} &= R_s|_{\tau=0}\end{aligned}\right\} \implies \widetilde{M_s}\approx\widetilde{r}\cdot\frac{\alpha}{a_i\widetilde{\tau}} \implies \widetilde{\tau}\approx\frac{\alpha\widetilde{r}}{a_i\widetilde{M_s}}. \tag{A31}$$

The mutual dependence of the variables in Eq. (3) is reversed to express $\tau = \tau(R_s)$,

$$\tau(R_s) = \left[1-\left(\frac{R_s}{\widetilde{r}}\right)^{\frac{1}{\alpha}}\right]\widetilde{\tau}, \tag{A32}$$

and therefore $\tau(R_s)$ [from Eq. (A32)] and $\widetilde{\tau}$ [from Eq. (A31)] are substituted into Eq. (A30),

$$M_s = \frac{\alpha R_s}{a_i\widetilde{\tau}\left\{1-\left[1-\left(\frac{R_s}{\widetilde{r}}\right)^{\frac{1}{\alpha}}\right]\right\}} = \left(\frac{\alpha\widetilde{r}^{\frac{1}{\alpha}}}{a_i\widetilde{\tau}}\right)R_s^{\frac{\alpha-1}{\alpha}}, \tag{A33}$$

to obtain, from the intermediate passage of Eq. (A31),

$$R_s = \left(\frac{M_s}{\widetilde{M_s}}\right)^{\frac{\alpha}{\alpha-1}}\widetilde{r}. \tag{A34}$$

Equation (A34) is then substituted into the expressions of ϕ [Eq. (A26)] and λ [Eq. (A27)]. The final expression of the correlation between the local values of M_s and θ_w^P,

$$\theta_w^P = \theta_w^P(M_s), \tag{A35}$$

is reported in Table II.

[1] V. Eliasson, N. Apazidis, and N. Tillmark, "Controlling the form of strong converging shocks by means of disturbances," Shock Waves **17**, 29–42 (2007).

[2] G. Guderley, "Starke kugelige zylindrische verdichtungsstöße in der nähe des kugelmittelpunktes bzw. der zylinderachse," Luftfahrtforschung **19**, 302–312 (1942).

[3] D. S. Butler, "Converging spherical and cylindrical shocks," Report 54/54, Armament Research and Development Establishment, Ministry of Supply, 1954.

[4] G. Ben-Dor, *Shock Wave Reflection Phenomena* (Springer, 1995).

[5] F. Vignati and A. Guardone, "Leading edge reflection patterns for cylindrical converging shock waves over convex obstacles," Phys. Fluids **28**, 096103 (2016).

[6] E. Mach, "Über den verlauf von funkenwellen in der ebene und im raume," Sitzungsbr. Akad. Wiss. Wien **78**, 819–838 (1878).

[7] R. Courant and K. O. Friedrichs, *Supersonic Flow and Shock Waves* (Wiley, Inc., New York, 1948).

[8] L. G. Smith, "Photographic investigation of the reflection of plane shocks in air," OSRD Report 6271, Office of Scientific Research and Development, Washington, DC, 1945.

[9] D. R. White, "An experimental survey of the mach reflection of shock waves," Technical Report II-10, Princeton University, Department of Physics, 1951.

[10] M. J. Lighthill, "The diffraction of blast. I," Proc. R. Soc. A **198**, 454–470 (1948).

[11] P. Colella and L. F. Henderson, "The von Neumann paradox for the diffraction of weak shock waves," J. Fluid Mech. **213**, 71–94 (1990).

[12] K. P. Stanyukovich, *Unsteady Motion of Continuous Media* (Gostekhizdat, Moscow, 1955), pp. 804–878.

[13] G. Ben-dor and K. Takayama, "Analytical prediction of the transition from Mach to regular reflection over cylindrical concave wedges," J. Fluid Mech. **158**, 365–380 (1985).

[14] K. Takayama and M. Sasaki, "Effects of radius of curvature and initial angle on the shock transition over concave and convex walls," Rep. Inst. High Speed Mech. **46**, 1–30 (1983).

[15] G. Ben-Dor and K. Takayama, "Application of steady shock polars to unsteady shock wave reflections," AIAA J. **24**, 682–684 (1986).

[16] H. Schlichting, *Boundary-Layer Theory* (McGraw-Hill Series in Mechanical Engineering, 1979).

[17] V. Eliasson, M. Kjellander, and N. Apazidis, "Regular versus Mach reflection for converging polygonal shocks," Shock Waves **17**, 43–50 (2007).

[18] D. Isola, A. Guardone, and G. Quaranta, "Arbitrary Lagrangian Eulerian formulation for two-dimensional flows using dynamic meshes with edge-swapping," J. Comput. Phys. **230**, 7706–7722 (2011).

[19] D. Isola, A. Guardone, and G. Quaranta, "Finite-volume solution of two-dimensional compressible flows over dynamic adaptive grids," J. Comput. Phys. **285**, 1–23 (2015).

[20] F. Vignati and A. Guardone, "Multi-domain simulations of shock wave interaction with aerodynamic obstacles in cylindrical implosions," J. Comput. Appl. Math. **283**, 218–227 (2015).

[21] F. Vignati and A. Guardone, "Dynamics of cylindrical converging shock waves interacting with aerodynamic obstacle arrays," Phys. Fluids **27**, 066101 (2015).

[22] D. C. Montgomery and G. C. Runger, *Applied Statistics and Probability for Engineers*, 5th ed. (John Wiley & Sons, 2010).

[23] J. O. Langseth and R. J. LeVeque, "A wave propagation method for three-dimensional hyperbolic conservation laws," J. Comput. Phys. **165**, 126–166 (2000).

[24] W. Chester, "The quasi-cylindrical shock tube," London, Edinburgh, Dublin Philos. Mag. J. Sci. **45**, 1293–1301 (1954).

[25] R. F. Chisnell, "The formation of a shock wave in a channel," J. Fluid Mech. **2**, 286–298 (1955).

[26] G. B. Whitham, "A new approach to the problems of shock dynamics. Part 1. Two-dimensional problems," J. Fluid Mech. **2**, 146–171 (1957).

[27] G. B. Whitham, *Linear and Nonlinear Waves* (John Wiley & Sons, New York, 1973).

[28] M. Kjellander, N. Tillmark, and N. Apazidis, "Thermal radiation from a converging shock implosion," Phys. Fluids **22**, 046102 (2010).

[29] D. W. Schwendeman and G. B. Whitham, "On converging shock waves," Proc. R. Soc. A **413**, 297–311 (1987).

[30] S. Itoh, N. Okazaki, and M. Itaya, "On the transition between regular and Mach reflection in truly non-stationary flows," J. Fluid Mech. **108**, 383–400 (1981).

[31] W. H. Heilig, "Diffraction of a shock wave by a cylinder," Phys. Fluids **12**, I-154–I-157 (1969).

[32] E. W. Skews and J. T. Ashworth, "The physical nature of weak shock wave reflection," J. Fluid Mech. **542**, 105–114 (2005).

[33] A. M. Tesdall, R. Sanders, and B. Keyfitz, "Self-similar solutions for the triple point paradox in gasdynamics," J. Appl. Math. **68**(5), 1360–1377 (2008).